Research Paper in *International Journal for Multiscale Computational Engineering* **RESEARCH GATE**

DOI: 10.1615/IntJMultCompEng.2021040212
Link (forthcoming paper): https://www.dl.begellhouse.com/journals/61fd1b191cf7e96f,forthcoming,40212.html

A concurrent micro/macro FE-model optimized with a limit analysis tool for the assessment of dry-joint masonry structures

Marco F. Funari[1], Luís C. Silva[2], Nathanael Savalle[1], Paulo B. Lourenço[1]

[1]University of Minho, ISISE, Guimarães, Portugal. E-mail: marcofrancesco.funari@civil.uminho.pt, n.savalle@civil.uminho.pt, pbl@civil.uminho.pt

[2]Lusófona University, ISISE, Lisbon, Portugal. E-mail: luis.silva@ulusofona.pt

Abstract

A two-step strategy for the mechanical analysis of unreinforced masonry (URM) structures, either subjected to in- and out-of-plane loading, is presented. At a first step, a semi-automatic digital tool allows the parametric modeling of the structure that, together with an Upper bound limit analysis tool and a heuristic optimization solver, enables tracking the most prone failure mechanism. At a second step, a coupled concurrent FE model with micro- and macro-scales is assumed. A micro-modeling description of the masonry is allocated to regions within the failure mechanism found in the former step. In converse, the other domain regions are modeled via a macro-approach, whose constitutive response is elastic and orthotropic and formulated through closed-form homogenized-based solutions. The application of the framework is based on non-linear static (pushover) analysis and conducted on three benchmarks: (i) an in-plane loaded URM shear wall; (ii) a U-shaped URM structure; and (iii) a URM church. Results are given in terms of load capacity curves, total displacement fields, and computational running time; and compared against those found with a FE microscopic model and with a limit analysis tool. Lastly, conclusions on the potential of the framework and future research streams are addressed.

Keywords: Masonry, Micro-modeling, Macro-modeling, two-step approach, Homogenization, URM Applications, Concurrent FE model

1 Introduction

Field inspections after earthquake events report how out-of-plane failure mechanisms are prone to occur in historical masonry structures. Undesired consequences include the collapse of buildings, human losses, and loss of societal identity (Stepinac et al., 2021; Vlachakis et al., 2020). Preventive remedial interventions on the built heritage are complex to perform since a sound knowledge of the structural and material features is lacking for most of the cases. Scientifically based studies are less susceptible to inadequate actions and advocate for proper structural analysis tools. To this aim, the literature was, in the last decades, enriched with the development of analysis methods for masonry structures. A plethora of strategies can be found now but seems clear that research leans towards the so-called (i) analytical and (ii) numerical approaches (Ferreira et al., 2014; Ferreira et al., 2015; D'Altri et al., 2019).

Analytical approaches are often based on the theorems of limit analysis and through a force- or displacement-based formulation (Cascini et al., 2018; Gianmarco de Felice et al., 2001). These are especially suitable for a rapid seismic fragility assessment, as require few input material parameters and provide good estimations on collapse load multiplier for defined failure mechanisms (Giuffré 1996; D'Ayala, and Speranza 2003); however, are unable to track displacement history and damage evolution. To what concerns numerical approaches, the Finite Element Method (FEM) (Fortunato et al., 2017; Aşıkoğlu et al., 2019) and the Discrete Element Method (DEM) (Savalle et al., 2020; Lemos, 2007; Lemos, 2019; Bui et al., 2017; Gonen et al., 2021) are largely used. DEM is now well suited for masonries with both dry- and mortared joints, but still requires a full representation of the blocks (masonry units) arrangement (Lemos, 2007). FEM allows a more versatile application as masonry can be represented either through a continuous equivalent media (designated macro-modeling) or by a discrete representation of units and joints (designated micro-modeling). Linear and non-linear static and dynamic analyses are eligible. Nonetheless, additionally to the significant amount of data needed to characterize the non-linear response of materials, the analysis can be both time-consuming and computationally expensive when estimating the ultimate ductility level of the structure.

To cope with the prohibitive computational cost, especially when dealing with large-scale structures and within full material nonlinearity, multi-scale FE methods seem a promising alternative and are in between the micro- and macro- FE schemes. Classical FE^2 approaches, i.e. the full continuum-FE methods, have clear advantages if linear elastic behavior is assumed, but obtaining a micro-scale solution at each load step of a non-linear process for each Gauss point may turn the problem prohibitive from a computational point of view; especially if nonlinearities are assumed (Otero et al., 2015; Lourenço et al., 2020). These strategies still have a higher computational cost than a FE macroscopic model. Hence full continuum-based FE^2 approaches are seldom used for dynamic purposes and complex structural analysis (Lourenço et al., 2020). The development of techniques that keep accuracy to acceptable levels and speed up the processing running times is critical. Several authors tried, therefore, to address simplifications on two-step frameworks.

The use of discrete FE-based methods at a macro-level is a promising alternative. Two-step approaches based on a discrete FE-based at a macro-scale are very practical due to the decrease of the number of degrees of freedom (comparing to a continuous approach) and are especially useful to perform dynamic analysis. Several studies have shown the clear advantages of this process since it allows a good trade-off between consumed time and results' accuracy and enables the study of real scale buildings. The latter is even more clear if simplifications are further assumed at both macro- or micro-scales, as observed in (Gabriele Milani et al., 2011; Bertolesi et al., 2019; Sharma et al., 2021; Casolo et al., 2013; Silva et al., 2017).

The use of limit analysis can be also a promising alternative. Some authors used a kinematic theorem of limit analysis at a macro-level to obtain the homogenized failure surfaces with a very limited computational effort (Cecchi et al., 2008; G. Milani et al., 2006; de Buhan et al., 1997). Such methods give a lower or upper bound estimate on the failure collapse load that can be scarce in some cases. Nonetheless, limit analysis is also being used together with FE-based strategies. Recently, Betti and Galano (2012) and Cundari et al. (2017) proposed similar frameworks, in which the global structural analysis was achieved by non-linear static or dynamic analysis aiming at the detection of the most likely collapse mechanisms. Then, at a second step, an upper bound limit analysis method was applied in the identified mechanisms to compute the maximum horizontal acceleration that the structure can withstand. Additionally, Funari et al. (2020) developed a non-linear static analysis to identify the most prone failure mechanisms and then, in a second step, aimed to refine the geometry of the failure mechanism through an optimization based on limit analysis and genetic algorithm; hence exploring an extensive set kinematically compatible solutions. D'Altri, et al. (2021) used limit analysis as a first step towards the identification of cracked surfaces and, in the next step, a macroscopic FE model was used to perform non-linear quasi-static analysis, in which the cracking zones were simulated with a microscopic description. However, a full-nonlinear behavior for the whole structure (even for the non-cracked zone) was assumed, which blurs the computational efficiency of the procedure and especially highlights the interest over more sophisticated approaches.

In this endeavor for a fast tool, yet able to give accurate descriptions of the structure's capacity and damage evolution, one may stress the so-called concurrent multi-scale approaches. These have been already applied to simulate fracture propagation in composites (Talebi et al. 2015; Ghosh 2015), nanocomposite (Ren et al. 2016), but also in the study of masonry structures (Lorenzo Leonetti et al., 2018; Driesen et al., 2021; Lourenço et al., 2020). A concurrent multiscale approach contemplates two well-separated scales, i.e. refined and coarse domains, described by a non-conforming mesh discretization and solved simultaneously. The refined domain, which ensures the modeling of non-linearities in the material behavior, is adopted in the regions that expect to fail, whereas, in the coarse domain, non-linearities are assumed negligible.

Lloberas-Valls et al. (2012a) investigated several incompatible mesh connections in the framework of a strongly coupled multiscale model to describe the crack growth and coalescence phenomena. Their model integrated a sophisticated zoom-in procedure that enables, during the loading history and based on a proper mechanical criterion, to switch from a coarser to a finer discretization of the media. Similarly, Talebi et al. (2015) developed a concurrent coupling scheme suitable to simulate the crack and dislocations at an atomistic level. Rodrigues et al. (2018) focused on the definition of an adaptive concurrent multiscale approach for the crack propagation phenomena in concrete structures. Their main novelty lies in using a non-periodic RVE cell, in which the FE mesh between the refined and coarse domains are independent.

A noteworthy study of a concurrent multiscale approach to investigate the in-plane failure of masonry structures was developed by Leonetti et al. (2018). A multiscale/multidomain-based computational scheme allowed to reduce the computational cost associated with a classical FE micro-modeling approach. Furthermore, a recent study on the subject has shown the potential of multiscale approaches applied to masonry in a bi-dimensional framework and pointed out, as a future research path, the interest of limit analysis envisioned as a preliminary step for this kind of procedure (Driesen et al., 2021).

The literature shows the potential of two-step procedures. However, the development of such tools aiming at an optimal localization of non-linearities – to reduce the associated convergence issues and computational cost – is still needed. Although concurrent multiscale approaches are certainly a promising alternative to simulate the failure of an extensive range of materials, e.g. concrete, masonry, composites, among others, its use is still limited to bi-dimensional frameworks and for small-scale case studies. In this context, this paper presents an integrated two-stepped procedure that was developed with the aim of enriching the literature on the field of FE concurrent model. The main contribution is the possibility of conducting a three-dimensional analysis of masonry structures within a low computational cost. To this aim, at a first step, a limit analysis tool finds the most prone failure mechanisms. At a second step, a FE concurrent multiscale approach is used to study the in-plane and out-of-plane response of masonry structures. Both steps are coupled, meaning that the failure surfaces that are found with limit analysis are modeled within a microscopic approach. Furthermore, and to fully optimize running times, the domain that is beyond the cracking surfaces, from an a-priori given characteristic length, is modeled as an elastic and orthotropic media.

The paper is organized into four main sections: section 2 describes the analysis framework focusing on both theoretical and numerical aspects; section 3 reports three validation examples, which differ in scale, and reports the benchmark given as a case study; and finally, final remarks are discussed in Section 4.

2 Two-scale framework: general description

A numerical framework is presented aiming an accurate description of the in- and out-of-plane mechanical behavior of unreinforced masonry (URM) structures. It was formulated to require a lower computational cost than full FE microscopic and macroscopic (non-linear) strategies (Roca et al., 2013; Lourenço et al., 2020). The so-called concurrent approach (firstly presented by Fish (2006)) is adopted together with a limit analysis tool. In this regard, the framework has two sequential and coupled steps, in which a limit analysis is conducted first, and a concurrent FE analysis is employed next.

The framework described in more detail next includes three main tasks, as given in Figure 1, needed to compute the mechanical response of URM structures. The first step consists of the geometric modeling of the structure via an explicit representation of both masonry units and joints (micro-modeling approach). In the second step, masonry units are merged, and its topology is optimized to provide a macro representation of the media. Prone in-plane and/or out-of-plane failure mechanisms are a-priori assigned, and the location of the yielding surfaces is optimized by an upper bound limit analysis theorem coupled with a heuristic solver. At this stage, the third step is conducted, in which an ad-hoc script represents the sub-structure activated by the failure mechanism through a micro-scale representation. The outer domain, i.e. the rest of the structure that is not involved in the mechanism, keeps a macro and continuous representation. Finally, the concurrent FE multiscale model can be used to perform the structural assessment of the structure through linear/non-linear quasi-static/dynamic type of analysis and within a FE environment. Further details over each step are addressed in the next sections.

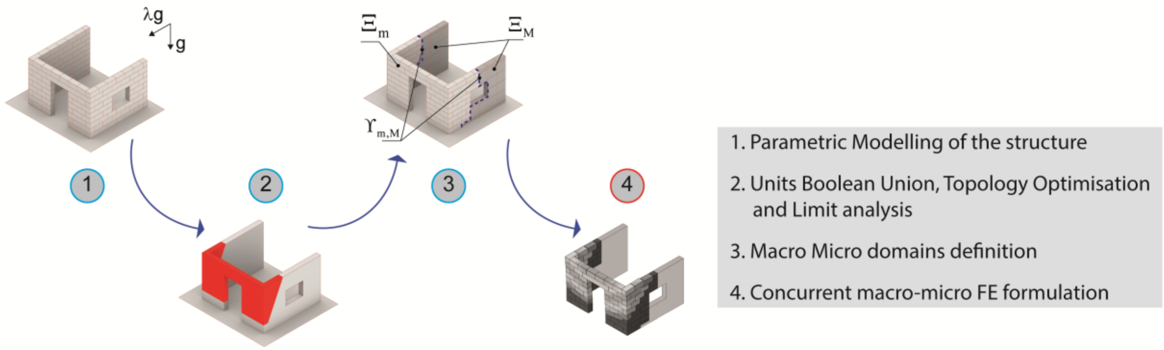

Figure 1: Schematic representation of the proposed two-step numerical strategy.

2.1 Parametric modelling of the structure

The geometric modeling of the structure is the first step of the framework (node one in Figure 1). To this aim, it requires the knowledge of the masonry arrangement since a micro-modeling approach is assumed. Although a full representation of masonry units and joints can be cumbersome and time-consuming, the framework integrates a digital tool that was recently proposed by Savalle, et al. (2021). This tool allows the pre-processing of the geometry via an automatic generation of the masonry arrangement, and it was implemented in the environment offered by Rhinoceros (+ Grasshopper) through C# programming language. It includes an initial discretization of the structure into elementary parts, i.e. walls arrangement, location of corners, location of T-connection, among other substructures, which can be assembled without any restriction aiming to form complex three-dimensional structures. Then, by setting up the dimensions of units and joints – given as user input –, the masonry pattern is positioned to respect the latter structural features. Openings can be also included in the walls, and the user can specify its height, length, position, and the dimension of lintels. For the sake of brevity, the reader is referred to (Savalle et al., 2021) for further details.

2.2 Upper-Bound Limit Analysis

The geometric model defined in the first step serves as a basis to conduct the second step of the framework. In this sub-step of the framework, prone failure mechanisms are pre-defined and assessed through an optimization tool that integrates an Upper-Bound limit analysis theorem coupled with a heuristic solver (node two in Figure 1). Therefore, the geometry of the expected active failure mechanism is parametrized to find the optimal configuration. The optimization problem aims at the minimization of the horizontal load multiplier, which can be formulated through the principle of virtual work. Figure 2 describes an overturning mechanism of a masonry wall, in which the kinematic description required to formulate the problem is conditioned by one virtual rotation δ_θ (Casapulla, et al. 2014; Funari, et al. 2020). The formulation of such a mechanism is addressed next, as it is the one assumed for the benchmarks reported in this study. It worth stressing that the formulation resorts on a representation of the media through a macro-approach – units forming the masonry prototype are merged –, in which the mechanism is represented by one virtual parameter only (Figure 2). Such assumption is convenient for an initial assessment of the most prone mechanism, and it is largely used in classic limit analysis approaches, see for instance (Sorrentino et al., 2017; D'Ayala et al., 2002).

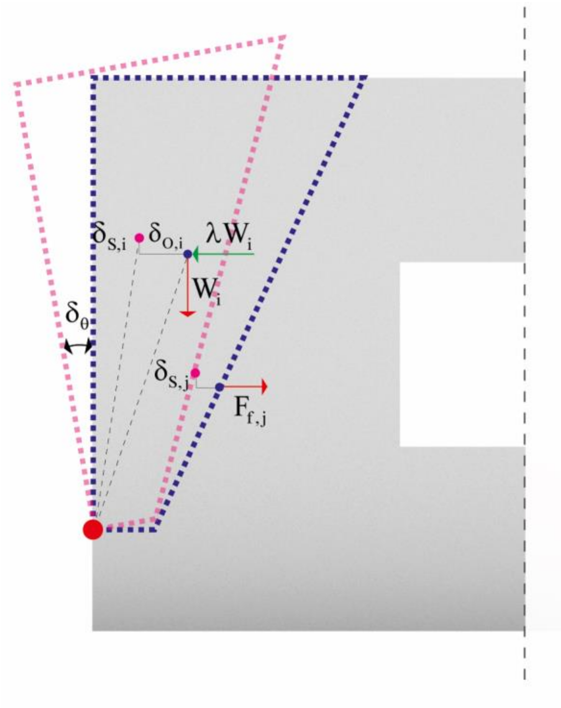

Figure 2: Kinematic description of the overturning failure mechanism.

As presented in Figure 2, the external virtual work contains both the overturning as well as the stabilizing works performed by the inertial forces, whereas the internal work derives from the friction force at contact interfaces:

$$\begin{aligned} \delta W_{ext} &= \lambda \sum_{i=1}^{n} W_i \delta_{O,i} - \sum_{i=1}^{n} W_i \delta_{S,i} \\ \delta W_{int} &= \sum_{j=1}^{n} F_{f,j} \delta_{S,j} \end{aligned} \tag{1}$$

in which W_i are the inertial forces arising from the self-weight of the $i-th$ masonry wall and including as well the contribution of roof and floors; $\delta_{O,i}$ and $\delta_{S,i}$ are the virtual overturning or stabilizing displacements of the application point of the inertial forces (that coincides with the virtual centroid if self-weight is considered only); $F_{f,j}$ are the frictional forces computed as a weighted value of the maximum friction force F_{max} based on the inclination of the crack line, as given next (Casapulla et al., 2014):

$$F_f = F_{max}\left(1 - \frac{\alpha_c}{\alpha_b}\right) \tag{2}$$

Here, α_b and α_c are the maximum frictional and crack angle, respectively (Funari, Mehrotra, and Lourenço 2021). The value of the horizontal load multiplier λ is obtained by solving Eq. (1) and reads:

$$\lambda = \frac{\sum_{j=1}^{n} F_{f,j}\delta_{S,j} + \sum_{i=1}^{n} W_i \delta_{S,i}}{\sum_{i=1}^{n} W_i \delta_{O,i}} \quad (3)$$

It is worth noting that the value λ depends on the geometry of the failure mechanism, which is defined by the crack inclination α_c and the height of the rotational hinge H_h. Such variables define the set of possible λ values. At last, the optimization of the out-of-plane failure mechanism geometry is achieved by solving the following constraint minimization problem:

$$\begin{cases} \min \ \lambda : \begin{bmatrix} \tan\alpha_{min} \leq \tan\alpha_c \leq \tan\alpha_b \\ 0 \leq H_h \leq H_W \end{bmatrix} \end{cases} \quad (4)$$

The constrained optimization problem defined in Eq. (4) was numerically implemented in a GHPython script, as depicted in Figure 3. Input data include: (i) the geometry defined in the first step (node one in Figure 1), (ii) the friction coefficient of the masonry, (iii) the rotational axis, and (iv) the geometric dimensions of masonry units. As shown in Figure 3, the variables of the optimization problem are grouped in the magenta box, i.e.: (i) the slope of the crack surfaces, and (ii) the height of the rotational axis. The solution is achieved using the GH component Galapagos (Rutten, 2013), in which a heuristic research method based on a genetic algorithm is implemented. The optimization problem finds the configuration for the critical failure mechanism and under a low processing time (few seconds). The kinematic problem used herein has theoretical background on the works of Turco, et al. (2020); Funari, et al. (2020).

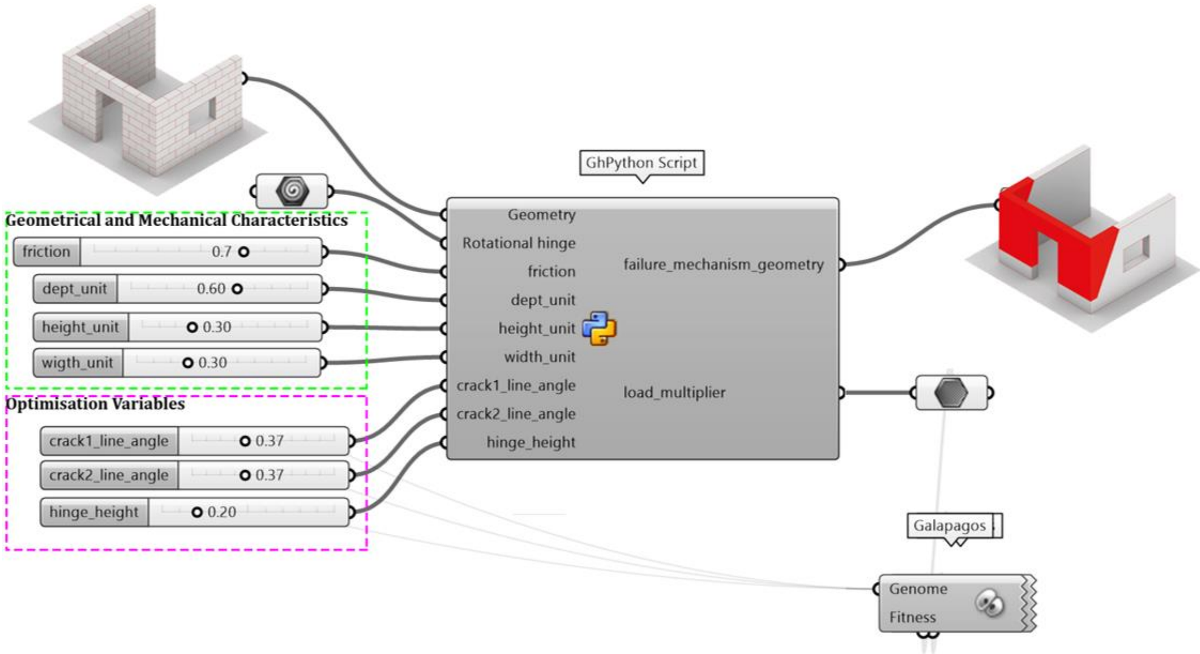

Figure 3: Limit analysis tool implemented in Rhino+Grasshopper through GHPython scripting that finds the critical failure mechanism.

2.3 Macro-Micro domains definition

The definition of macro- and micro-domains is the third step of the framework (node three in Figure 1). It resumes being a fast procedure once the theoretical failure mechanism is found by limit analysis. The decomposition of both domains is directly defined over the failure mechanism. Although other re-meshing approaches would be plausible, the present study assumes two different scales. A finer scale, designated as micro-domain Ξ_m that is attributed to the substructure defined by the active failure mechanism, in which masonry arrangement is explicitly represented. A coarser scale, designated as macro domain Ξ_M is attributed to the rest of the structure, in which masonry is represented through a continuous and equivalent elastic media.

A contentious issue is the finding of the frontier between domains. Cracking tends to spread from the main surfaces failures and have an important role in the non-linear behavior of masonry and in damage-induced orthotropy. To avoid inaccurate solutions retrieved from the disregard of this cracking, the damage in the vicinity of the main failure surfaces was considered by adding the scalar parameter R as input. The parameter R is a length value that extends the part of the structure being characterized with a microdomain, as presented in Figure 4. The choice of R affects both the accuracy and computational time of the solution since it increases or decreases the non-linear region of the model. Therefore, a proper choice of R-value is paramount and it is recommended that it includes: (i) the epistemic error in the prediction of the hinges through limit analysis, (ii) the existence of a potential curved failure surface, in converse to the straight-type yielded surfaces assumed by the limit analysis tool, and (iii) the more diffuse failure surfaces due to the zig-zag damage (especially in sliding and flexure mechanisms) in actual masonry specimens (Restrepo Vélez et al., 2014; Bui et al., 2017; Cascini et al., 2018).

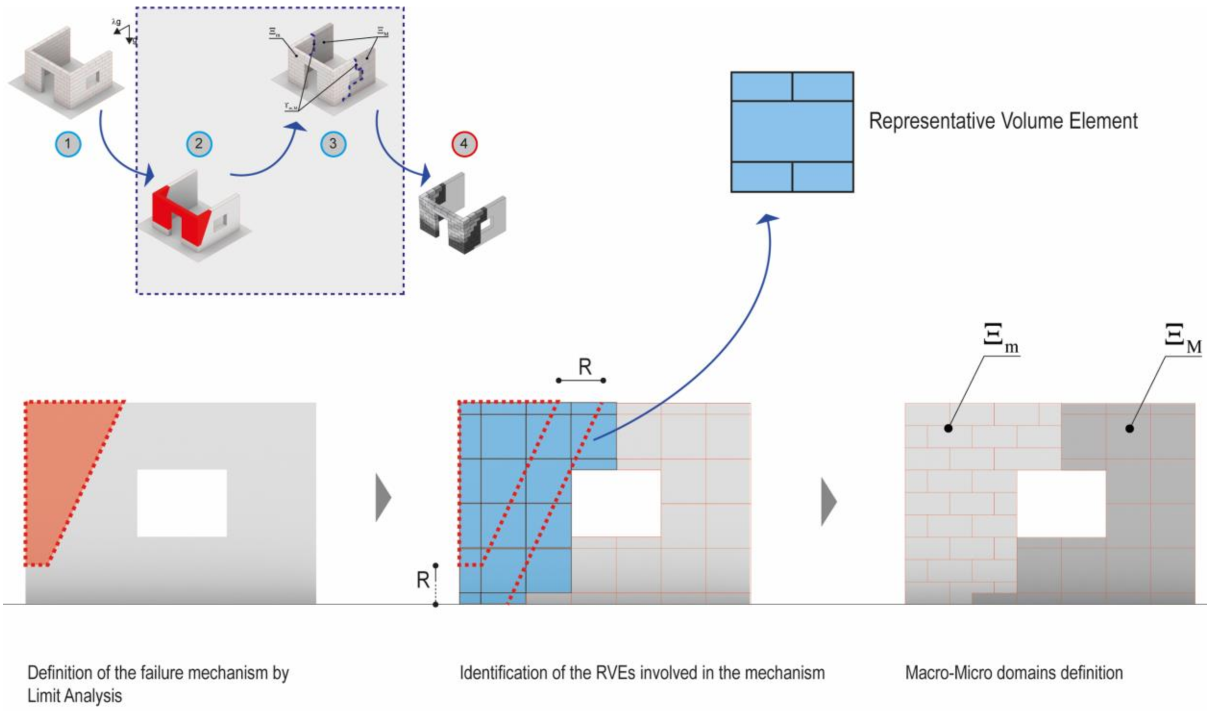

Figure 4: Schematic representation of the decomposition procedure into macro- and micro-domains.

In this regard, and as schematically described in Figure 4, the dimension of the Representative Volume Element (RVE) defines the grid that enables the domain decomposition. This resorts to be an alike strategy followed by other studies, as (Vandoren et al., 2013; Lorenzo Leonetti et al., 2018; Alessandri et al., 2015; Almeida et al., 2020; Lloberas-Valls et al., 2012; Driesen et al., 2021). A classical RVE adopted for a running-bond pattern (Trovalusci et al., 2015) was considered since the selected case studies follow such arrangement; needless to state that other configurations can be employed. The domain decomposition of every grid region, into a micro-description of the RVE, is performed if intersect the failure surface (plus the characteristic length *R*); being the other grid elements kept as macro domain Ξ_{M} regions.

2.4 Concurrent FE macro-micro model

The limit analysis procedure performed over the structure allows identifying two subdomains that have different scales of computation, i.e. the macroscopic Ξ_{M} and the microscopic Ξ_{m} domains (Figure 1, node 3). Both are concurrent, meaning that together define simultaneously different volumes of the structure. Towards a low computational cost, material non-linearities are assigned only to the materials belonging to the micro-domain Ξ_{m}. On the other hand, the media inside the Ξ_{M} domain is simulated with an equivalent linear elastic orthotropic material, whose elastic properties are computed with a proper homogenization strategy to guarantee the objectivity of the solution. Such hypotheses are particularly suitable for well-marked failures, as the ones experienced in unreinforced masonry structures: local failure mechanisms governed by out-of-plane loading due to poor connection between structural elements (Malena et al., 2019; Restrepo Vélez et al., 2014).

2.4.1 Variational Formulation

The concurrent FE model requires a numerical solution for each scale and was implemented in the FE software Abaqus (2014). A set of weak form equations are solved in a coupled manner through a variational formulation for both the Ξ_{M} and the Ξ_{m} domains. Proper kinematic constraints are employed at the regions where both domains meet, designated as interfaces $\Upsilon_{\mathrm{m,M}}$. Specifically, an additional internal boundary condition is associated with $\Upsilon_{\mathrm{m,M}}$ and seeks to enforce the continuity between total displacement (Lorenzo Leonetti et al., 2018; Driesen et al., 2021):

$$
\begin{aligned}
&\Xi_M: \quad \int_{\Xi_M} \boldsymbol{\sigma}_{\mathbf{M}}\, \boldsymbol{\delta\varepsilon}_{\mathbf{M}} \mathrm{d}\Xi_M - \int_{\Upsilon_{m,M}} \zeta \cdot \boldsymbol{\delta}\mathbf{u}_{\mathbf{M}} \mathrm{d}\Upsilon_{m,M} = \int_{\Xi_M} \mathbf{B}_{\mathbf{M}}^{\mathbf{T}} \cdot \boldsymbol{\delta}\mathbf{u}_{\mathbf{M}} \mathrm{d}\Xi_M + \int_{\Upsilon} \mathbf{p}_{\mathbf{M}}^{\mathbf{T}} \cdot \boldsymbol{\delta}\mathbf{u}_{\mathbf{M}} \mathrm{d}\Upsilon \\
&\Xi_m: \quad \int_{\Xi_m} \boldsymbol{\sigma}_m\, \boldsymbol{\delta\varepsilon}_m \mathrm{d}\Xi_m + \int_{\Upsilon_m} \mathbf{t} \cdot \ddot{\mathbf{u}}_{\mathbf{m}} \cdot \boldsymbol{\delta}\ddot{\mathbf{u}}_{\mathbf{m}} \mathrm{d}\Upsilon_m + \int_{\Upsilon_{m,M}} \zeta \cdot \boldsymbol{\delta}\mathrm{u}_{\mathbf{m}} \mathrm{d}\Upsilon_{m,M} = \int_{\Xi_m} \mathbf{B}_{\mathbf{m}}^{\mathbf{T}} \cdot \boldsymbol{\delta}\mathbf{u}_{\mathbf{m}} \mathrm{d}\Xi_m + \int_{\Upsilon} \mathbf{p}_{\mathbf{m}}^{\mathbf{T}} \cdot \boldsymbol{\delta}\mathbf{u}_{\mathbf{m}} \mathrm{d}\Upsilon \qquad (5) \\
&\Upsilon_{m,M.}: \quad \int_{\Upsilon_{m,M}} \delta\zeta\left(\mathbf{u}_{\mathbf{m}} - \mathbf{u}_{\mathbf{M}}\right) \mathrm{d}\Upsilon_{m,M} = 0
\end{aligned}
$$

in which $\mathbf{u}_{\mathbf{M}}$ and $\mathbf{u}_m$ are the displacement fields belonging to the $\Xi_{\mathbf{M}}$ and $\Xi_{\mathbf{m}}$ subdomains, respectively. Υ_m represent the interfaces of the micro-domain and Υ represent the boundaries with applied external forces (surface tractions or nodal forces). $\mathbf{B}_m$ and $\mathbf{B}_M$ are the vectors containing the body loads along with the three global cartesian directions, p_m and p_M are the vectors of the surfaces loads active on the boundary, ζ is the Lagrange load multiplier of the forces that control the residual interface gap across adjacent domains, $\boldsymbol{t}$ is the traction force acting at the interfaces within the Ξ_M domain, and $\ddot{\mathbf{u}}_{\mathbf{m}}$ is the displacement jump at the Υ_m interfaces (Figure 5).

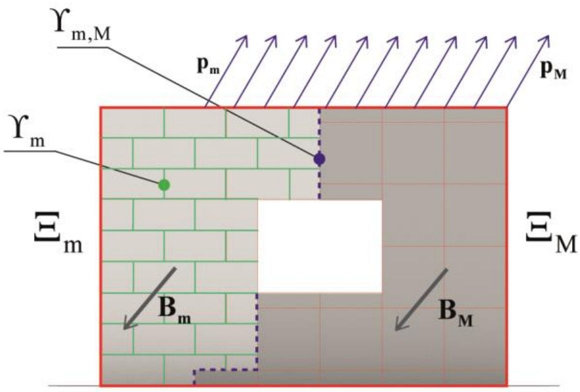

Figure 5: Schematic representation of the variational formulation of the concurrent FE numerical approach.

Equation (5) defines the concurrent FE multiscale approach that is solved within an explicit scheme available in ABAQUS (Abaqus, 2014). The static solution is obtained by dynamic relaxation, using scaled masses and artificial damping. To this aim, the energy balance is continuously evaluated and to guarantee that the kinetic energy of the deforming media is below a small fraction of the total internal energy (1–5%) (Abaqus, 2014). The latter condition must hold to guarantee the objectivity of the results through an explicit procedure. In this context, smooth step amplitude curves and a small-time increment allow reaching appropriate results.

2.4.2 Micro-domain numerical model

Masonry units are assumed to be deformable discrete blocks following an isotropic and linear elastic constitutive law (E_u , ν_u). Joints are represented by zero-thickness interfaces, which include a non-associative plastic flow rule and a classical Mohr-Coulomb failure surface criterion. Normal and tangential contact behaviors (stress-displacement laws) assume an infinitesimal interpenetration between blocks. A linear relationship between the over-closure displacements and the applied stress is defined by the normal k_n and tangential k_s stiffness values. A friction coefficient (f) defines the plastic slipping criterion in shear within a penalty approach, in which a perfectly plastic response occurs after reaching the critical shear stress. For the present case study, only dry mortar type of masonry is studied and, therefore, cohesion has been neglected when representing joint interfaces (in tension and shear regimes).

According to the distinct element method, a local damping factor is considered. The equations of motion are damped to reach a force equilibrium state as quickly as possible under the applied initial and boundary conditions. Damping is velocity-proportional (magnitude of the damping force is proportional to the velocity of the blocks) and it was assumed equal to 0.8 in the present study. The adopted FE software is Abaqus (2014) contains the latter mentioned contact interface model. The constitutive law is automatically assigned to all the interfaces of the micro-domain Ξ_m through the General Contact algorithm (Abaqus, 2014).

2.4.3 Macro-domain numerical model

The macro-domain Ξ_M represents masonry through an orthotropic linear elastic media. According to the theory of elasticity, the spatial stiffness matrix for an orthotropic material is defined by a 6×6 symmetric matrix, which is fully determined through nine engineering constants, i.e. three elastic moduli E_{XX}, E_{YY}, E_{ZZ}, three Poisson's ratios ν_{XY}, ν_{XZ}, ν_{YZ}, and three shear moduli G_{XY}, G_{XZ}, G_{YZ}, associated with the principal directions (Figure 6).

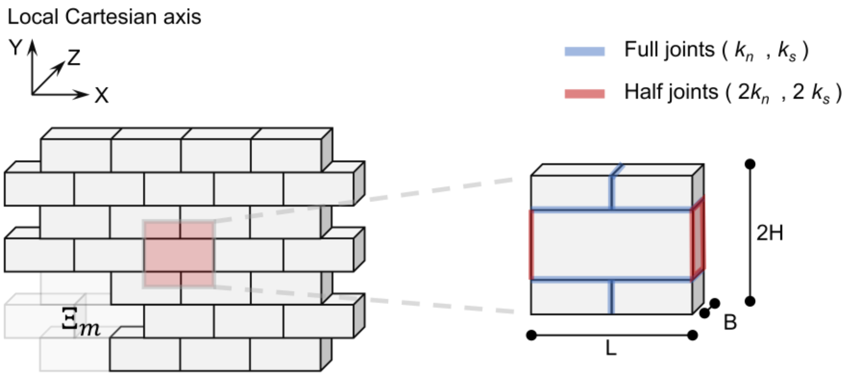

Figure 6: Representative Volume Element (RVE) for the homogenization procedure of the macro-domain Ξ_M.

A closed-form solution was found to define the material elasticity matrix of a running-bond dry-joint masonry. It was inspired in the works of Kouris et al. (2020) for a two-dimensional media, in which a set of equivalent springs represent the in-plane response of a mortared masonry RVE. Herein, the equivalent three-dimensional elastic response is defined by ad-hoc expressions formulated based on the representation of a set of springs to describe the masonry, as presented in Figure 7. Since contact interfaces are being used to characterize the numerical behavior of dry-mortar joints, the springs given in Figure 7 correspond to surfaces in the numerical model (unit of Pressure/Length). Parameters L, H, and B denote the unit length (X), height (Y), and width (Z), respectively; hence the RVE's height is given as 2H and length given by L (Figure 7). An assemblage of springs is conceived aiming at the representation of a system equivalent to a running-bond masonry RVE. Since a dry-joint masonry will be studied only, the compression range is the one that is analyzed here being the RVE subjected to compression stress σ for mode-I deformation modes. The computed elastic homogenized properties are described in terms of equivalent Young's moduli, Shear moduli, and Poisson’s coefficients.

Figure 7 presents the latter assumptions. More detail on the formulation is given in Appendix 1.

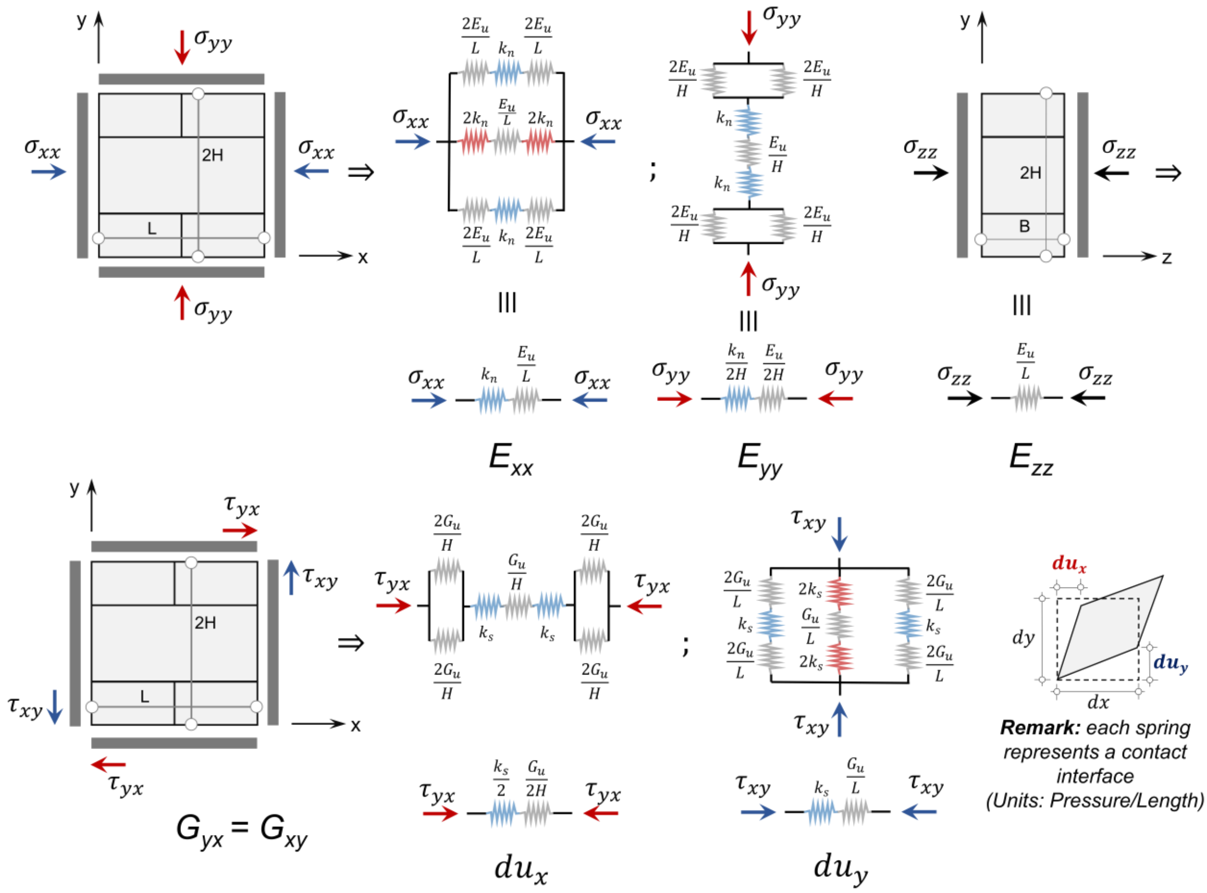

Figure 7: Strategy followed to compute the equivalent elastic properties of the masonry RVE: Young's moduli and shear moduli (details for the Poisson’s ratio are given in Appendix A).

Table 1 summarizes the closed-form expression to compute the elastic properties of the equivalent linear elastic orthotropic material; the reader is referred to (Kouris et al., 2020) for further theoretical details within an alike procedure. The mechanic-based formulation adopted has clear simplifications, but brings advantages related to the ease of computational implementation. Nonetheless, among the more sophisticated models available in the literature, only a few deal with dry-joint masonries, and the majority are devoted to 2D frameworks (G. de Felice et al., 2010).

Table 1: Equivalent homogenized elastic properties for a running-bond masonry RVE (orthotropic material).

Young's modulus	Poisson's ratio	Shear modulus
$E_{xx} = \frac{Lk_n E_u}{E_b + Lk_n}$	$\nu_{xz} = \nu_{xy} = -\frac{\varepsilon_{zz}}{\varepsilon_{xx}} = \nu_u \frac{E_{xx}}{E_u}$	$G_{xy} = \frac{HLk_s G_u}{G_u(H+L) + 2HLk_s}$
$E_{yy} = \frac{Hk_n E_u}{E_u + Hk_n}$	$\nu_{zx} = \nu_{zy} = \nu_u$	$G_{xz} = \frac{Lk_s G_u}{G_u + 2Lk_s}$
$E_{zz} = E_u$	$\nu_{yx} = \nu_{yz} = \nu_u \frac{E_{zz}}{E_u}$	$G_{zy} = \frac{Hk_s G_u}{G_u + 2Hk_s}$

2.4.4 Micro and macro interfaces

The concurrent FE model included two domains – macro Ξ_M and micro Ξ_m – that embody the structure numerical model and represent the mechanical behavior of masonry. These domains are assigned to different volumes and meet in different regions by sharing a common surface interface $\Upsilon_{m,M}$. Such interface $\Upsilon_{m,M}$ is characterized by two-adjoining boundaries with different scale representations for the masonry and FE mesh sizes ranging $\Delta_M / \Delta_m \approx 10$, in which Δ_M and Δ_m are the characteristic FE mesh size of the Ξ_M and Ξ_m domains, respectively.

Interfaces $\Upsilon_{m,M}$ must link adjoining non-conforming FE meshes. Contact points (or nodes) of each boundary are set into two families, defined as: CP_i, which corresponds to the contact points located on the Ξ_M domain only; and the CP_d, which is the set of contact points that are paired between Ξ_M and Ξ_m domains. The continuity of the displacement between CP_d is imposed through a Lagrange multiplier functional. For CP_i, the Lagrange multiplier can be achieved following several procedures, e.g. approximation through shape functions. Figure 8 represents this concept in the case of a two-dimensional problem for the sake of simplicity, but the interpolation occurs in two orthogonal directions because the proposed strategy is processed in the three-dimensional space. From a numerical standpoint, such kinematic conditions are implemented by means of a tie constraint algorithm, which is available in Abaqus (2014). Therefore, the assumption of total displacement continuity between the two domains is guaranteed, even though the FE mesh are non-concordant.

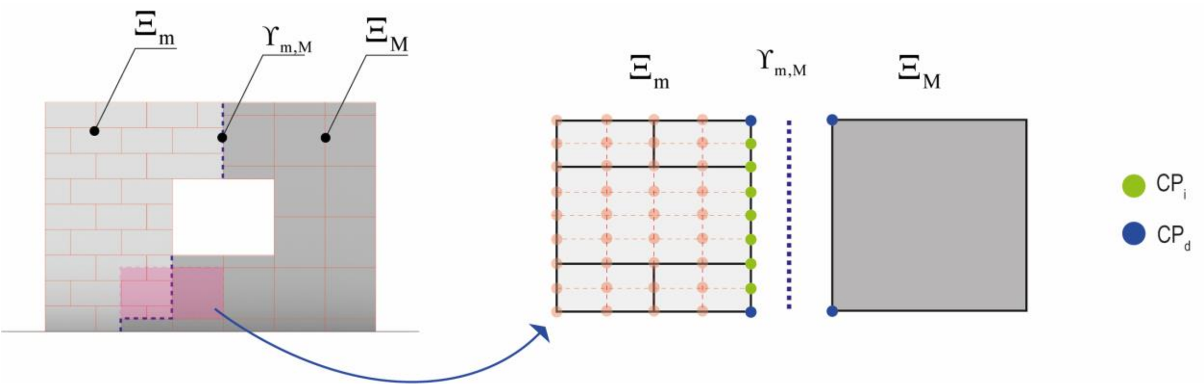

Figure 8: Concurrent FE model and localization of the interface $\Upsilon_{m,M}$ that link the macro- and micro-domains with the corresponding contact points.

3 Two-scale framework: numerical application

The numerical application of the proposed two-step framework is conducted over three case studies, which include small to large-scale structures. Aiming to validate the strategy, the results found are compared against a microscopic model, hereafter named as RMM (reference microscopic model). The RMM is one the most accurate (and computationally expensive) numerical strategies at disposal in the literature and serves, therefore, as a reference method for validation purposes.

The first case study is a dry-joint masonry wall with an opening and subjected to an in-plane shear load. The second case study addresses three connected dry-stone masonry walls within a U-shape plan arrangement (Smoljanović et al., 2018). It aims to explore the potential of the proposed approach when the structures are affected by coupled in-plane and out-plane mechanisms. Finally, the third case study is a large-scale monumental building, whose geometry is inspired by the Church of San Nicolò Capodimonte located in Camogli (Genova, Italy) (Funari, Mehrotra, and Lourenço 2021).

3.1 Small-scale structure: URM shear wall

The first case study concerns a dry-joint masonry shear wall. The wall is fixed at the base and its geometry is given in Figure 9. Two load cases are applied in a sequent manner: the self-weight is applied first, and a lateral body force (mass proportional) is applied next through an incremental load factor λ, as presented in Figure 9 (node 1). Material properties required to complete the proposed procedure are given in

Table 2, specifically the material density (ρ) and friction coefficient (f) for the limit analysis procedure; the Young's modulus and the Poisson's coefficient of the masonry units to define the overall elastic orthotropic matrix of the Ξ_M domain according to the closed-form solutions of section 2.4.3; and the normal and tangential stiffness values for the micro-macro interfaces. The dimensions of units are $0.80 \times 0.35 \times 0.40 \mathrm{m}^3$ $(\mathrm{L} \times \mathrm{H} \times \mathrm{B})$.

Table 2: Mechanical properties adopted in the RMM and proposed CMM for the URM shear wall study.

ρ [kg m^{-3}]	f	E_u [Pa]	ν_u	k_n [Pa m^{-1}]	k_s [Pa m^{-1}]
2000	0.7	10x10^9	0.2	1x10^9	1x10^9

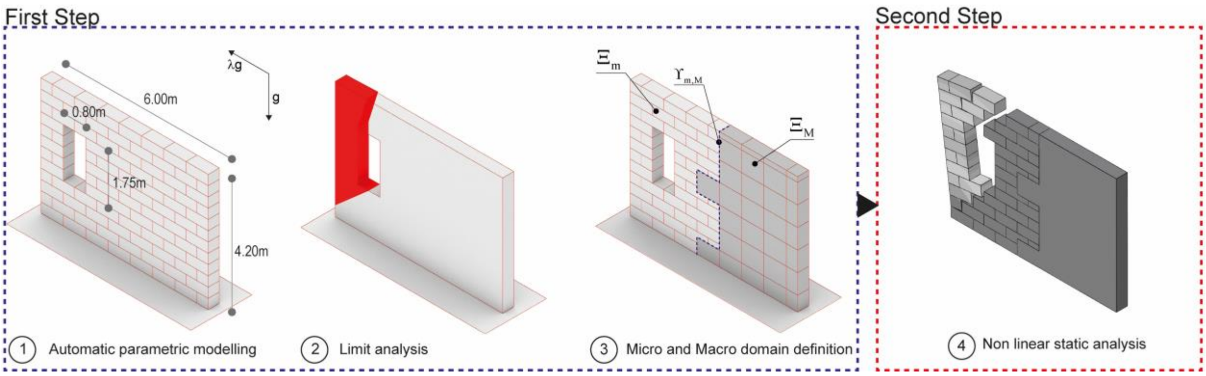

Figure 9: Proposed two-step framework applied to the URM shear wall case study.

The proposed strategy is employed – as addressed in section 2 –, in which the modeling of the wall was achieved by a semi-automatic parametric micro-modeling, and a limit analysis tool applied next aiming the detection of the most prone failure mechanism geometry for the given loading conditions. The limit analysis uses a heuristic procedure embedded in the Galapagos solver (Rutten, 2013) and converged to a load multiplier value equal to $\lambda = 0.219$ (meaning an equivalent shear base force of 0.219.g, in which g is the gravitational acceleration). The obtained failure mechanism, linked with the third sub-step of the proposed algorithm as remarked in Figure 1, follows a re-meshing procedure to define the two non-overlapping domains, i.e. the micro Ξ_m and the macro Ξ_M domains. The characteristic length R was assumed to be $R = 2L$ (L is the length of the masonry unit that, for the dry-joint masonry of this case study, matches the length of the RVE). Note that the failure defined by limit analysis can have a jagged profile that may be caused, for instance, by the presence of openings.

The transfer between the first processing step, i.e. the limit analysis, with the second processing step of the framework, i.e. the structural analysis by a concurrent FE model, is performed through a Python script (The Python Language Reference — Python 3.9.5 Documentation, 2021). It allows the automatic creation of the numerical FE model within Abaqus CAE environment (Abaqus, 2014), in which both domains are properly represented. Masonry units that belong to the Ξ_m domain are discretized by eight-node linear hexahedral finite elements (C3D8R in Abaqus (2014)); thus leading to a $\Delta_m / \kappa = 1/2$, in which $\kappa = \min\ (L, B, H)$. In the Ξ_M domain, a coarser mesh (structured FE mesh with squared elements) was adopted with a $\Delta_{M.} / L = 1$, meaning that the FE size is 0.80m to match the length of masonry units.

Results of the proposed CMM and RMM are presented in Figure 10, both in terms of lateral load-displacement capacity (node with maximum displacement as control node) and total displacement map at collapse ($\lambda = 0.220$). The comparison of the results allows demonstrating that the proposed approach ensures a good solution accuracy. Furthermore, it is noteworthy to highlight that the CMM allows saving 58% of the computational time cost required by the RMM.

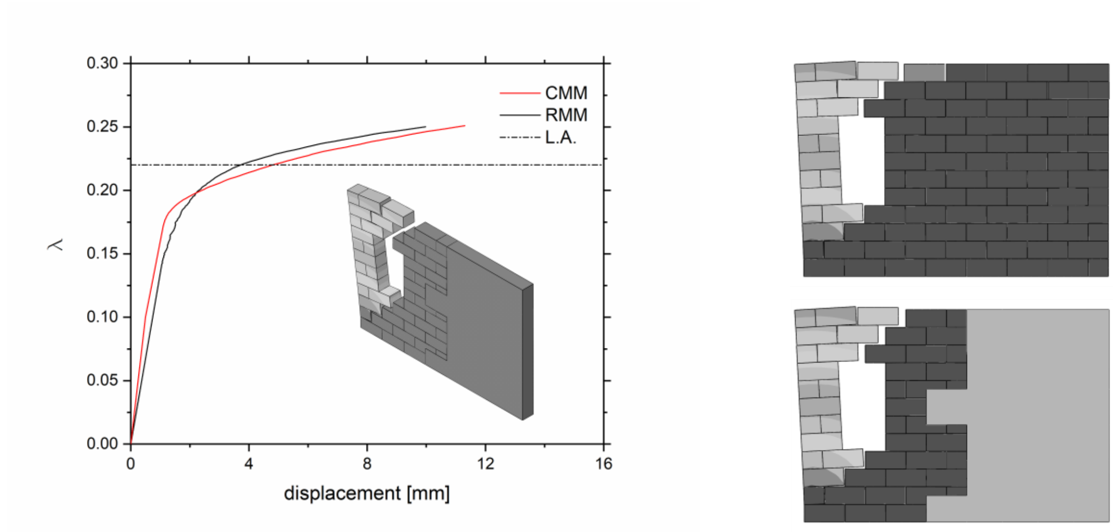

(a) (b)

Figure 10: Results obtained for the in-plane loaded masonry wall: (a) lateral load-displacement relationship; and (b) displacement map for the RMM and proposed CMM.

3.2 Small-to-medium scale structure: U-shaped URM walls

The second case study concerns a URM structure composed of three walls within a U-shaped plan arrangement. It is based on the Smoljanović, et al. (2018) works and brings more complexity than the former case study since both in- and out-of-plane co-exist. Walls are fixed at the base and the geometry of the structure is given in Figure 11. Two load cases are applied in a sequent manner: the self-weight is applied first, and a lateral body force (mass proportional) is applied next through an incremental load factor λ, as presented in Figure 11 (node 1). The lateral force is orthogonal to the façade wall and then following its out-of-plane direction.

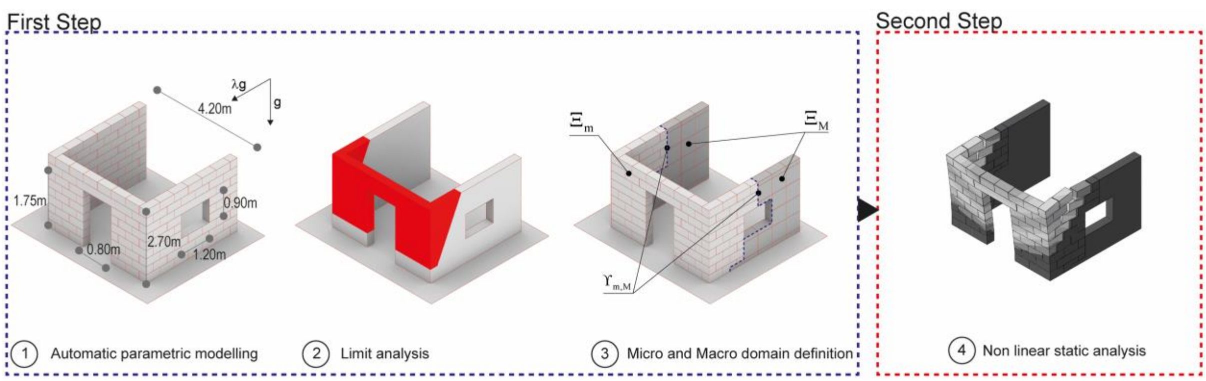

Figure 11: Proposed two-step framework applied to the U-shaped URM case study.

Material properties required to complete the proposed procedure are given in Table 3: the material density (ρ) and friction coefficient (υ) for the limit analysis procedure; the Young's modulus and Poisson's coefficient of masonry units to define the overall elastic orthotropic matrix of the Ξ_M domain according to the closed-form solutions of section 2.4.3; and the normal and tangential stiffness values for the micro-macro interfaces. The dimensions of units are $0.60 \times 0.30 \times 0.30 m^3$ $(L \times H \times B)$.

Table 3: Mechanical properties adopted in the RMM and proposed CMM for the U-shaped URM structure studied by Smoljanović, et al. (2018).

ρ [kg m^{-3}]	E_u [Pa]	ν_u	k_n [Pa m^{-1}]	k_s [Pa m^{-1}]	f
2000	10x10^9	0.2	1x10^9	1x10^9	0.7

The proposed strategy is employed and the obtained failure mechanism through limit analysis is given in Figure 11 (node 2), in which the out-of-plane mechanism of the main façade governs the collapse mode. The numerical FE concurrent model (CMM) is then developed at Abaqus CAE environment (Abaqus, 2014) by a re-meshing procedure that retrieves two non-overlapping domains, i.e. the micro Ξ_m and the macro Ξ_M domains. A characteristic length R was assumed to be $R = 2L$ (L is the length of the masonry unit that, for the dry-joint masonry of this case study, matches the length of the RVE). Masonry units that belong to the Ξ_m domain are discretized by eight-node linear hexahedral finite elements (C3D8R in Abaqus (2014)); thus leading to a $\Delta_m / \kappa = 1/2$, in which $\kappa = \min(L, B, H)$. In the Ξ_M domain, three mesh refinements (structured FE mesh with squared elements) were evaluated to assess the trade-off between accuracy-computational achieved. To this aim, the following FE mesh ratios were adopted: (i) CMM-M1, with a finer FE mesh and size given by $\Delta_M / \kappa = 1/2$; (ii) CMM-M2, an in-between mesh refinement with a size given by $\Delta_M / L = 1/2$; and (iii) CMM-M3, with a coarser FE mesh and size given by $\Delta_M / L = 1$.

Furthermore, the influence of the parameter R was investigated. Note that R is a parameter (units of length) that directly affect the volumes of both micro- and macro-domains (see section 2.4.2). Therefore, an additional model designated as CMM-M3-R was also considered: it has a FE mesh size for the Ξ_M domain given by $\Delta_M / L = 1$ and an R=L (half-value of the other CMM models).

Results from the proposed CMM and RMM are presented in Figure 12. Lateral load-displacement capacity curves (node with maximum displacement as control node) in Figure 12a show slight differences in the elastic range, yet negligible from a structural engineering standpoint as are within a 5% bound. CMM model is slightly stiffer than the RMM, especially in the linear range, and it may be explained due to the loss of accuracy that macro-modeling offers when compared with a micro-modeling approach. Nonetheless, differences are unnoticeable when plastic deformations govern the response; is noteworthy to highlight that the CMM micro-domain is responsible for such deformation. Collapse occurs for a load-factor around $\lambda = 0.295$ for all the studied numerical models. It is important to point out that the collapse instant is defined when the kinematic energy is higher than 5% of the total energy because an explicit formulation was adopted. In such a context, the results allow demonstrating that the proposed approach ensures a promising solution accuracy. Furthermore, it is noteworthy to highlight that the CMM allows saving 58% of the computational time cost required by the RMM.

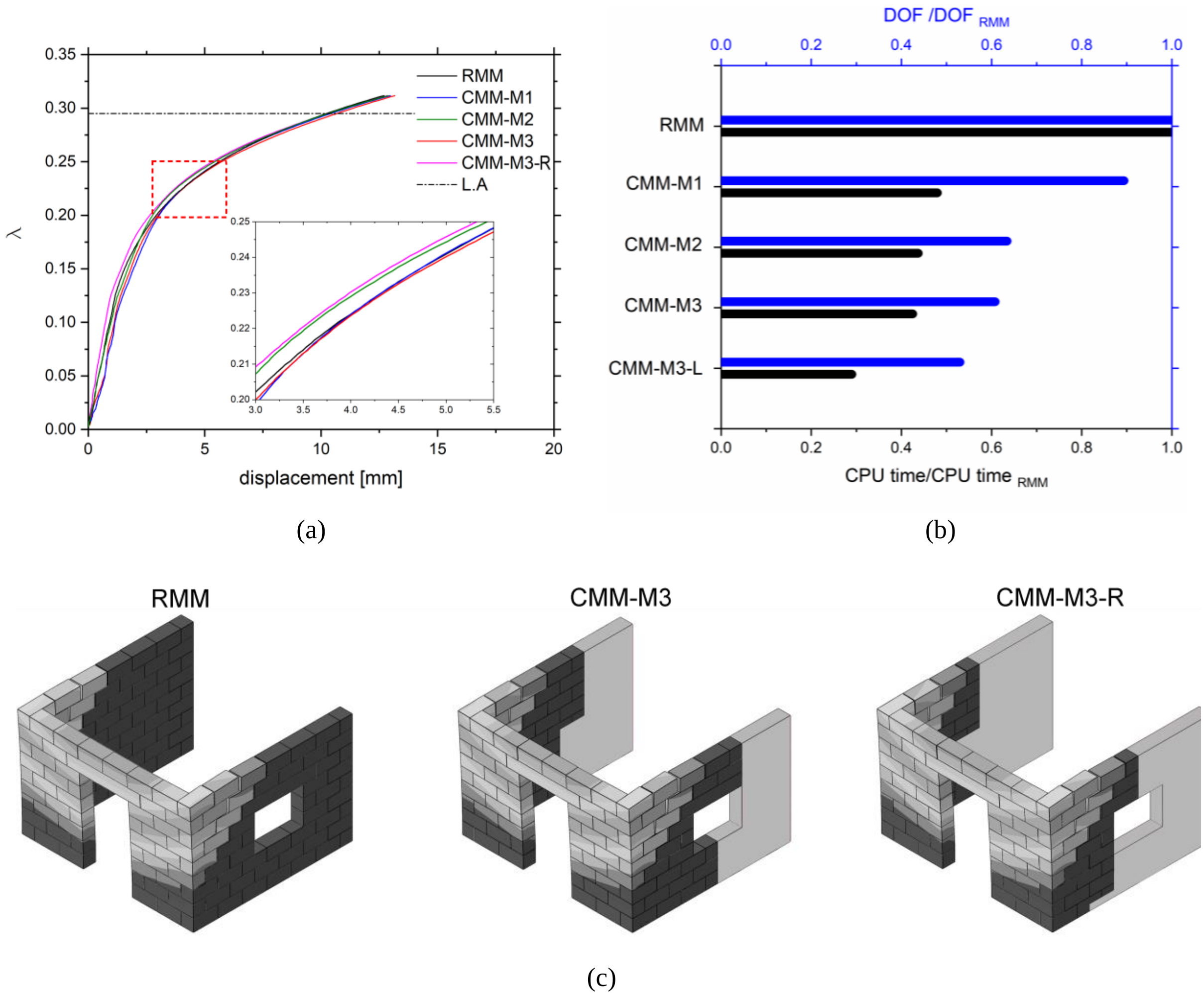

Figure 12: Results obtained for the U-shaped URM structure: (a) lateral load-displacement relationship; (b) computational time (CPU) and number of degrees-of-freedom (DOFs) for each numerical simulation; and (c) displacement map for the RMM and proposed CMM-M3 and CMM-M3-R.

Figure 12b reports a comparison including the required computational time (CPU) and the number of degrees-of-freedom (DOFs) for each numerical model. Despite CMM-M1, CMM-M2 and CMM-M3 have clear differences in the number of DOF, differences in the required CPU time are minimal and allow saving around 60% of the time in comparison with the RMM. In this regard, the approach seems to not suffer from a substantial mesh bias at the Ξ_M domain; this holds at least for FE mesh sizes with a dimension lower than the RVE size. On the other hand, Figure 12b allows doing an important finding, i.e. the parameter R has a significant impact since it allows decreasing 10% of the required CPU time when compared to the CMM-M3. Therefore, this parameter must be assessed with care. It allows improving the computational time, but decreasing its value may also compromise the accuracy level. The authors suggest a value bounded by $\mathrm{R} = \mathrm{L}$ to $\mathrm{R} = 2\mathrm{L}$.

The failure mechanisms obtained with the RMM, CMM-M3, and CMM-M3-R are summarized in Figure 12c through total displacement maps. The proposed FE concurrent models (for both R values) capture well the expected failure mechanism. At last, it is noteworthy to highlight that the proposed multi-scale framework returns promising results, in terms of load capacity curve and expected failure mechanism, while saving 65% of the computational time if compared to an accurate micro-modeling strategy (RMM).

3.3 Large-scale structure: URM church

The last case study – and the most complex one – concerns a URM church and aims to evaluate the promptness and accuracy of the two-step framework when applied for a large-scale structure. The URM church is characterized by a plan consisting of a Latin Cross (Funari, Mehrotra, and Lourenço 2021). The geometry of the church is given in Figure 13 and some important features can be addressed: the main façade wall has a total height of 14.0m and a base ranging 7.50m; the single bell tower is the tallest structural element, with a height of 17.0m; and the total length of the church is around 19.60m. Fixed boundary conditions are set at the base of the church walls. For the structural analysis, two load cases were considered and applied in a sequent manner: the self-weight is applied first, and a lateral body force (mass proportional) is applied next through an incremental load factor λ, as presented in Figure 11 (node 1). Such lateral force, which intends to be representative of a seismic excitation, was applied along the longitudinal direction of the church, as this is typically the weakest direction. Material properties required to complete the proposed procedure are given in Table 4: the material density (ρ) and friction coefficient (υ) for the limit analysis procedure; the Young's modulus and Poisson's coefficient of the masonry units to define the overall elastic orthotropic matrix of the Ξ_M domain according to the closed-form solutions of section 2.4.3; and the normal and tangential stiffness values for the micro-macro interfaces. The dimensions of units are $0.57 \times 0.275 \times 0.90\mathrm{m}^3$ $(L \times H \times B)$.

Table 4: Mechanical properties adopted in the RMM and proposed CMM for the URM church study.

ρ [kg m^{-3}]	f	E_b [Pa]	ν_b	k_n [Pa m^{-1}]	k_s [Pa m^{-1}]
2000	0.6	20×10^9	0.2	1×10^{11}	1×10^{11}

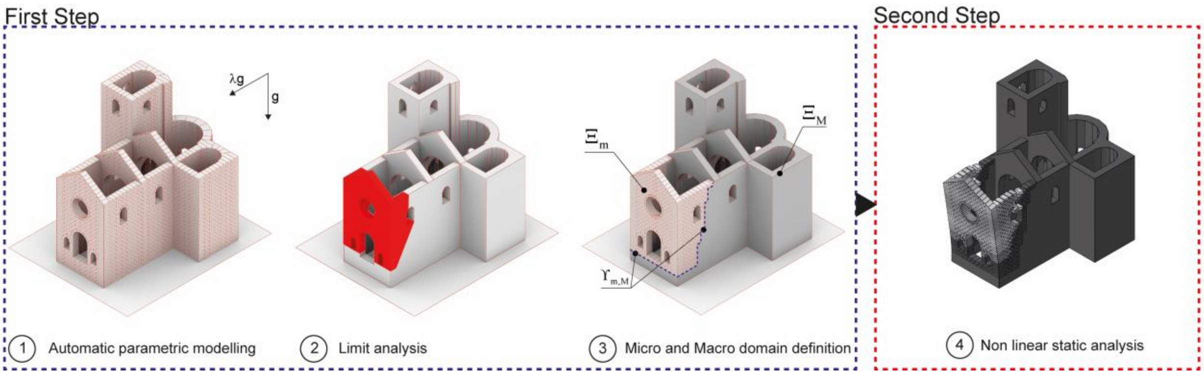

Figure 13: Proposed two-step framework applied to the URM church case study.

The proposed strategy is employed and the obtained failure mechanism through limit analysis is given in Figure 13 (node 2). The overturning mechanism of the gable wall of the church governs the collapse mode. Figure 13 (node 3) presents the corresponding numerical FE concurrent model (CMM) developed at Abaqus CAE environment (Abaqus, 2014) by a re-meshing procedure that retrieves the two non-overlapping domains, i.e. the micro Ξ_m and the macro Ξ_M . A characteristic length $R = 2L$ was assumed. Masonry units that belong to the Ξ_M domain are discretized by eight-node linear hexahedral finite elements (C3D8R in Abaqus (2014)); thus leading to a $\Delta_m / \kappa = 1/2$, in which $\kappa = \min\ (L, B, H)$. In the Ξ_M domain, a FE mesh refinement (structured FE mesh with squared elements) was considered with a size given by $\Delta_M / L = 1$.

Figure 14 summarizes the lateral load-displacement (pushover) curve found with the proposed CMM, together with the load multiplier value ($\lambda = 0.213$) of the limit analysis processed in the second sub-step (Figure 13) and with the numerical model from Malena, et al. (2019). The latter numerical model developed by Malena, et al. (2019) is based on a homogeneous macroscopic model with an elasto-plastic constitutive relation for the masonry.

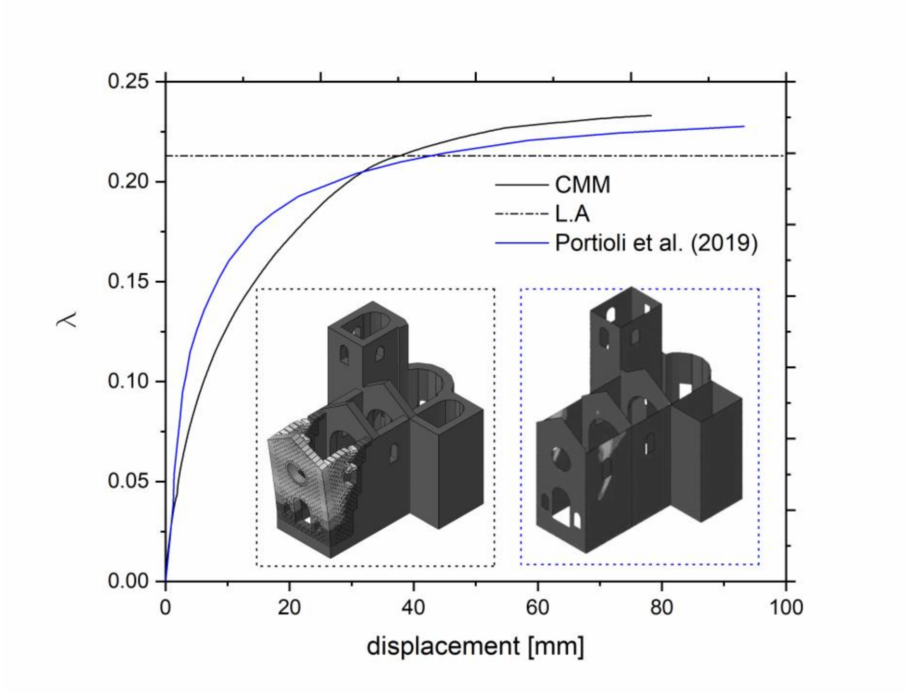

Figure 14: Results obtained for the URM church: lateral load-displacement (pushover) curve and displacement map for the proposed CMM and macroscopic model from Malena, et al. (2019).

The comparison of the results allows demonstrating that the proposed approach ensures a good solution accuracy, especially to what concerns the structure's load capacity. Some deviations still pose within the elastic range. The limit analysis allows predictions on the collapse load are within 8% difference. Figure 14 also gives the comparison in terms of failure mechanism. The proposed model offers a clear identification of the failure surfaces, as damage localization is directly lumped on FE interfaces. In converse, general insight over the failure mechanism is difficult to conduct with the macroscopic model used for comparison purposes; this is, however, a general disadvantage of macroscopic models that preclude a cracking-localization algorithm (Clemente et al., 2006). At last, it bears noticing that the proposed CMM has, within the micro-domain Ξ_m, a total of 800 masonry stone units that leads to a total CPU time of 75min. A comparison with a RMM was disregarded in this case study since the number of masonry units would increase up to more than 5000; meaning that a prohibitive CPU time would be required. No indication of CPU time required for the macroscopic model is reported in Malena, et al. (2019) and, therefore, a quantitative comparison on this matter is omitted.

4 Final remarks

A two-step procedure was proposed aiming at the in- and out-of-plane mechanical study of dry-joint masonry structures. At a first step, a semi-automatic digital tool allows the parametric modeling of the structure that, together with an upper bound limit analysis tool and a heuristic optimization solver, enables tracking the most prone failure mechanism. The time required to process the first step is limited to a matter of seconds. At a second step, a coupled three-dimensional concurrent FE model with micro- and macro-scales is assumed. A micro-modeling description of the masonry is allocated to regions activated by the failure mechanism found in the former step. The other regions of the domain are modeled via a macro-approach, whose constitutive response is elastic and orthotropic and based on closed-form homogenized-based solutions. The time required to complete the second step is conditioned by the scale of the structure and type of structural analysis performed, as the modeling of the concurrent FE model is automatic and takes a matter of seconds.

The application of the framework was achieved through non-linear quasi-static analysis on three benchmarks: (i) an in-plane loaded URM shear wall; (ii) a U-shaped URM structure; and (iii) a URM church. Results demonstrate the potential and advantages of the proposed approach. It was able to predict, with a marginal difference (lower than 1%), the collapse load value. Failure collapse modes resemble to be alike with the ones found with a microscopic FE model (first two case studies) and with a literature macroscopic FE model (for the third and last case study). Furthermore, the tool demonstrated that is quite attractive from a computational standpoint. It allows reducing the CPU time up to 60% in a small-to-medium scale structure (first and second case studies) when compared to a full microscopic FE model. Eventually, it may be the only alternative to macroscopic FE models when assessing large-scale structures, as micro-modeling proved to be a challenge.

At last, a comment on future research streams is of value. The two-step procedure is computational quite attractive, robust, and allows higher levels of accuracy. This is so because it is based on a sequential process in which a continuous transfer of information between scales is precluded during the analysis; as required in classical multi-domain strategies that need activation rules to process the macro-to-micro decomposition (L. Leonetti et al., 2018; Reccia et al., 2018; Driesen et al., 2021). Nonetheless, further studies need to be carried out to validate the approach in other contexts, for instance when assessing mortared masonry structures. In such a context, the authors believe that future works may include: (i) the definition of a more sophisticated limit analysis tool, e.g. (G. Milani, 2015; Chiozzi et al., 2017); and (ii) the implementation of an interfacial contact model at the micro-domain and within the FE concurrent model that can represent better the behavior of mortared joints (Lourenço et al., 2020).

5 Appendix

This appendix details the derivation of the formulas presented in Table 1, which have been formulated considering a spring's representation analogy (see Figure 7) and based on the infinitesimal strain theory.

The Young's modulus E_{xx}, E_{yy} and E_{zz} can be obtained following the same procedure. For the save of brevity, only E_{xx} component is addressed here. According to Hooke's law, the axial deformation and displacement read as:

$$E_{xx} = \frac{\sigma_{xx}}{\varepsilon_{xx}};\ \varepsilon_{xx} = \frac{\Delta u}{L};\ \Delta u = du_u + du_j \tag{A.1}$$

In which σ_{xx} is the axial load, ε_{xx} is the axial deformation, Δu is the total displacement of the RVE, du_u is the displacement component related to the unit, and du_j is displacement component related to the joints, i.e. its normal displacement (interpenetration). Both contact interfaces have the same applied uni-axial stress and, therefore, Equations A.1 reads as:

$$du_u = \frac{\sigma_{xx} L}{E_u};\ du_j = \frac{\sigma_{xx}}{k_n};\quad \frac{\sigma_{xx}}{L}\left(\frac{L}{E_u} + \frac{1}{k_n}\right) = \sigma_{xx}\left(\frac{k_n L + E_u}{E_u k_n L}\right) \tag{A.2}$$

Which corresponds to the following uni-axial Young's modulus E_{xx}:

$$E_{xx} = \frac{E_u k_n L}{k_n L + E_u} \tag{A.3}$$

For the in-plane shear moduli, one assumes the symmetry of the shearing stress components. Therefore, the in-plane shear moduli are defined as the ratio between the corresponding shear stress component and relative deformation. Accordingly:

$$G_{xy} = G_{yx} = \frac{\tau_{xy}}{\gamma_{xy}};\ \text{ with } \gamma_{xy} = \frac{du_x}{dy} + \frac{du_y}{dx} \tag{A.4}$$

The shearing deformation γ_{xy} $(= \gamma_{yx})$ should be computed when subjecting the RVE to a pure shear mechanism (Figure 7). Recalling that du_u is the shear displacement component related with the block deformation and du_j the shear displacement component related with the joint, the individual shearing deformation components are defined as:

$$\begin{aligned} \frac{du_x}{dy} &= \frac{du_u + du_j}{2H} = \frac{\tau_{yx}\left(\frac{2}{k_s} + \frac{2H}{G_u}\right)}{2H} = \tau_{yx}\frac{G_u + k_s H}{G_u k_s H} \\ \frac{du_y}{dx} &= \frac{du_u + du_j}{L} = \frac{\tau_{xy}\left(\frac{1}{k_s} + \frac{L}{G_u}\right)}{L} = \tau_{xy}\frac{G_u + k_s L}{G_u k_s L} \end{aligned} \tag{A.5}$$

By combining Eq. A.5 with Eq. A.4, one writes that the in-plane shear modulus is computed as:

$$G_{yx} = G_{xy} = \frac{1}{\frac{1}{2}\left(\frac{G_u + k_s H}{G_u k_s H} + \frac{G_u + k_s L}{G_u k_s L}\right)} = \frac{G_u k_s H L}{G_u(H+L) + 2k_s H L} \tag{A.6}$$

Lastly, the equivalent in-plane Poisson's ratio $\nu_{xy} = \nu_{yx}$ is demonstrated. To this aim, it bears highlighting that the lateral deformation in the joints was assumed to be zero since the study deals with dry-mortar masonries. Therefore, the subscript u is related to the unit only and the Poisson's ratio is given as:

$$\varepsilon_{xx,u} = \frac{\sigma_{xx}}{E_u} = \varepsilon_{xx}\frac{E_{xx}}{E_u};\ \varepsilon_{yy} = \varepsilon_{yy,u} = -\nu_u \times \varepsilon_{xx,u} = -\nu_u \varepsilon_{xx}\frac{E_{xx}}{E_u} \quad \text{(A.7)}$$

$$\nu_{yx} = \nu_{xy} = -\frac{\varepsilon_{yy}}{\varepsilon_{xx}} = \nu_u \frac{E_{xx}}{E_u} \quad \text{(A.8)}$$

6 References

Abaqus, V., 6.14 Documentation, *Dassault Systemes Simulia Corporation*, vol. **651**, no. 6.2, 2014.

Alessandri, C., Garutti, M., Mallardo, V. and Milani, G., Crack Patterns Induced by Foundation Settlements: Integrated Analysis on a Renaissance Masonry Palace in Italy, *International Journal of Architectural Heritage*, vol. **9**, no. 2, pp. 111–29, 2015. DOI: 10.1080/15583058.2014.951795

Almeida, F. P. A. and Lourenço, P. B., Three-Dimensional Elastic Properties of Masonry by Mechanics of Structure Gene, *International Journal of Solids and Structures*, vol. **191–192**, no. May, pp. 202–11, 2020. DOI: 10.1016/j.ijsolstr.2019.12.009

Aşıkoğlu, A., Avşar, Ö., Lourenço, P. B. and Silva, L. C., Effectiveness of Seismic Retrofitting of a Historical Masonry Structure: Kütahya Kurşunlu Mosque, Turkey, *Bulletin of Earthquake Engineering*, vol. **17**, no. 6, pp. 3365–95, from https://doi.org/10.1007/s10518-019-00603-6, 2019. DOI: 10.1007/s10518-019-00603-6

Bertolesi, E., Silva, L. C. and Milani, G., Validation of a Two-Step Simplified Compatible Homogenisation Approach Extended to out-Plane Loaded Masonries, *International Journal of Masonry Research and Innovation*, vol. **4**, p. 265, January 1, 2019. DOI: 10.1504/IJMRI.2019.10019407

Betti, M. and Galano, L., Seismic Analysis of Historic Masonry Buildings: The Vicarious Palace in Pescia (Italy), *Buildings*, vol. **2**, no. 2, pp. 63–82, April 2012. DOI: 10.3390/buildings2020063

Buhan, P. de and Felice, G. de, A Homogenisation Approach to the Ultimate Strength of Brick Masonry, *Journal of the Mechanics and Physics of Solids*, vol. **45**, no. 7, pp. 1085–1104, July 1997. DOI: 10.1016/S0022-5096(97)00002-1

Bui, T. T., Limam, A., Sarhosis, V. and Hjiaj, M., Discrete Element Modelling of the In-Plane and out-of-Plane Behaviour of Dry-Joint Masonry Wall Constructions, *Engineering Structures*, vol. **136**, no. October, pp. 277–94, 2017. DOI: 10.1016/j.engstruct.2017.01.020

Casapulla, C., Cascini, L., Portioli, F. and Landolfo, R., 3D Macro and Micro-Block Models for Limit Analysis of out-of-Plane Loaded Masonry Walls with Non-Associative Coulomb Friction, *Meccanica*, vol. **49**, no. 7, pp. 1653–78, from https://doi.org/10.1007/s11012-014-9943-8, 2014. DOI: 10.1007/s11012-014-9943-8

Cascini, L., Gagliardo, R. and Portioli, F., LiABlock_3D: A Software Tool for Collapse Mechanism Analysis of Historic Masonry Structures, *International Journal of Architectural Heritage*, pp. 1–20, from https://doi.org/10.1080/15583058.2018.1509155, September 5, 2018. DOI: 10.1080/15583058.2018.1509155

Casolo, S. and Milani, G., Simplified Out-of-Plane Modelling of Three-Leaf Masonry Walls Accounting for the Material Texture, *Construction and Building Materials*, vol. **40**, pp. 330–51, March 2013. DOI: 10.1016/j.conbuildmat.2012.09.090

Cecchi, A. and Milani, G., A Kinematic FE Limit Analysis Model for Thick English Bond Masonry Walls, *International Journal of Solids and Structures*, vol. **45**, no. 5, pp. 1302–31, 2008. DOI: 10.1016/j.ijsolstr.2007.09.019

Chiozzi, A., Milani, G. and Tralli, A., A Genetic Algorithm NURBS-Based New Approach for Fast Kinematic Limit Analysis of Masonry Vaults, *Computers & Structures*, vol. **182**, pp. 187–204, 2017. DOI: 10.1016/j.compstruc.2016.11.003

Clemente, R., Roca, P., and Cervera, M., Damage Model with Crack Localization–Application to Historical Buildings, *Structural Analysis of Historical Constructions*, New Delhi, India, pp. 1125–34, 2006.

Cundari, G. A., Milani, G. and Failla, G., Seismic Vulnerability Evaluation of Historical Masonry Churches: Proposal for a General and Comprehensive Numerical Approach to Cross-Check Results, *Engineering Failure Analysis*, vol. **82**, pp. 208–28, from http://www.sciencedirect.com/science/article/pii/S1350630717303187, 2017. DOI: https://doi.org/10.1016/j.engfailanal.2017.08.013

D'Altri, A. M., Sarhosis, V., Milani, G., Rots, J., Cattari, S., Lagomarsino, S., Sacco, E., Tralli, A., Castellazzi, G. and Miranda, S. de, Modeling Strategies for the Computational Analysis of Unreinforced Masonry Structures: Review and Classification, *Archives of Computational Methods in Engineering*, 2019. DOI: 10.1007/s11831-019-09351-x

D'Ayala, D. and Speranza, E., Definition of Collapse Mechanisms and Seismic Vulnerability of Historic Masonry Buildings, *Earthquake Spectra*, vol. **19**, no. 3, pp. 479–509, August 31, 2003. DOI: 10.1193/1.1599896

D'Ayala, D., and Speranza, E., An Integrated Procedure for the Assessment of Seismic Vulnerability of Historic Buildings, *12th European Conference on Earthquake Engineering*, October 16, 2002.

Driesen, C., Degée, H. and Vandoren, B., Efficient Modeling of Masonry Failure Using a Multiscale Domain Activation Approach, *Computers and Structures*, vol. **251**, p. 106543, July 2021. DOI: 10.1016/j.compstruc.2021.106543

Felice, G. de, Amorosi, A. and Malena, M., Elasto-Plastic Analysis of Block Structures through a Homogenization Method, *International Journal for Numerical and Analytical Methods in Geomechanics*, vol. **34**, no. 3, pp. 221–47, February 2010. DOI: 10.1002/nag.799

Felice, Gianmarco de and Giannini, R., Out-of-Plane Seismic Resistance of Masonry Walls, *Journal of Earthquake Engineering*, vol. **5**, no. 2, pp. 253–71, accessed May 22, 2018, from https://doi.org/10.1080/13632460109350394, 2001. DOI: 10.1080/13632460109350394

Ferreira, T. M., Costa, A. A. and Costa, A., Analysis of the Out-Of-Plane Seismic Behavior of Unreinforced Masonry: A Literature Review, *International Journal of Architectural Heritage*, vol. **9**, no. 8, pp. 949–72, November 10, 2014. DOI: 10.1080/15583058.2014.885996

Ferreira, T. M., Costa, A. A., Vicente, R. and Varum, H., A Simplified Four-Branch Model for the Analytical Study of the out-of-Plane Performance of Regular Stone URM Walls, *Engineering Structures*, vol. **83**, pp. 140–53, January 2015. DOI: 10.1016/j.engstruct.2014.10.048

Fish, J., Bridging the Scales in Nano Engineering and Science, *Journal of Nanoparticle Research*, vol. **8**, no. 5, pp. 577–94, 2006.

Fortunato, G., Funari, M. F. and Lonetti, P., Survey and Seismic Vulnerability Assessment of the Baptistery of San Giovanni in Tumba (Italy), *Journal of Cultural Heritage*, 2017. DOI: 10.1016/j.culher.2017.01.010

Funari, M. F, Spadea, S., Ciantia, M., Lonetti, P., and Greco, F., Visual Programming for the Structural Assessment of Historic Masonry Structures, *REHABEND*, 2020.

Funari, Marco F, Mehrotra, A. and Lourenço, P. B., A Tool for the Rapid Seismic Assessment of Historic Masonry Structures Based on Limit Analysis Optimisation and Rocking Dynamics, *Applied Sciences (Switzerland)*, vol. **11**, no. 3, pp. 1–22, February 2021. DOI: 10.3390/app11030942

Funari, Marco F, Spadea, S., Lonetti, P., Fabbrocino, F. and Luciano, R., Visual Programming for Structural Assessment of Out-of-Plane Mechanisms in Historic Masonry Structures, *Journal of Building Engineering*, vol. **31**, September 2020. DOI: 10.1016/j.jobe.2020.101425

Ghosh, S., Adaptive Hierarchical-Concurrent Multiscale Modeling of Ductile Failure in Heterogeneous Metallic Materials, *JOM*, vol. **67**, no. 1, pp. 129–42, January 2015. DOI: 10.1007/s11837-014-1193-7

Giuffré, A., A Mechanical Model for Statics and Dynamics of Historical Masonry Buildings, in *Protection of the Architectural Heritage Against Earthquakes*, Springer Vienna, pp. 71–152, 1996.

Gonen, S., Pulatsu, B., Erdogmus, E., Karaesmen, E. and Karaesmen, E., Quasi-Static Nonlinear Seismic Assessment of a Fourth Century A.D. Roman Aqueduct in Istanbul, Turkey, *Heritage*, vol. **4**, no. 1, pp. 401–21, 2021. DOI: 10.3390/heritage4010025

Kouris, L. A. S., Bournas, D. A., Akintayo, O. T., Konstantinidis, A. A. and Aifantis, E. C., A Gradient Elastic Homogenisation Model for Brick Masonry, *Engineering Structures*, vol. **208**, p. 110311, April 2020. DOI: 10.1016/j.engstruct.2020.110311

Lemos, J. V., Discrete Element Modeling of Masonry Structures, *International Journal of Architectural Heritage*, vol. **1**, no. 2, pp. 190–213, May 31, 2007. DOI: 10.1080/15583050601176868

Lemos, J. V., Discrete Element Modeling of the Seismic Behavior of Masonry Construction, *Buildings*, vol. **9**, no. 2, 2019. DOI: 10.3390/buildings9020043

Leonetti, L., Trovalusci, P. and Cechi, A., A Multiscale/Multidomain Model for the Failure Analysis of Masonry Walls: A Validation with a Combined FEM/DEM Approach, *International Journal for Multiscale Computational Engineering*, vol. **16**, no. 4, pp. 325–43, 2018. DOI: 10.1615/IntJMultCompEng.2018026988

Leonetti, Lorenzo, Greco, F., Trovalusci, P., Luciano, R. and Masiani, R., A Multiscale Damage Analysis of Periodic Composites Using a Couple-Stress/Cauchy Multidomain Model: Application to Masonry Structures, *Composites Part B: Engineering*, vol. **141**, pp. 50–59, May 2018. DOI: 10.1016/j.compositesb.2017.12.025

Lloberas-Valls, O., Rixen, D. J., Simone, A. and Sluys, L. J., On Micro-to-Macro Connections in Domain Decomposition Multiscale Methods, *Computer Methods in Applied Mechanics and Engineering*, vol. **225**–**228**, pp. 177–96, accessed August 31, 2017, from http://linkinghub.elsevier.com/retrieve/pii/S0045782512000989, June 2012. DOI: 10.1016/j.cma.2012.03.022

Lourenço, P. B. and Silva, L. C., Computational Applications in Masonry Structures: From the Meso-Scale to the Super-Large/Super-Complex, *International Journal for Multiscale Computational Engineering*, vol. **18**, no. 1, pp. 1–30, 2020. DOI: 10.1615/IntJMultCompEng.2020030889

Malena, M., Portioli, F., Gagliardo, R., Tomaselli, G., Cascini, L. and Felice, G. de, Collapse Mechanism Analysis of Historic Masonry Structures Subjected to Lateral Loads: A Comparison between Continuous and Discrete Models, *Computers and Structures*, vol. **220**, pp. 14–31, 2019. DOI: 10.1016/j.compstruc.2019.04.005

Maria D'Altri, A., Presti, N. Lo, Grillanda, N., Castellazzi, G., Miranda, S. de and Milani, G., A Two-Step Automated Procedure Based on Adaptive Limit and Pushover Analyses for the Seismic Assessment of Masonry Structures, *Computers and Structures*, vol. **252**, p. 106561, August 2021. DOI: 10.1016/j.compstruc.2021.106561

Milani, G., Upper Bound Sequential Linear Programming Mesh Adaptation Scheme for Collapse Analysis of Masonry Vaults, *Advances in Engineering Software*, vol. **79**, pp. 91–110, January 2015. DOI: 10.1016/J.ADVENGSOFT.2014.09.004

Milani, G., Lourenço, P. B. and Tralli, A., Homogenised Limit Analysis of Masonry Walls, Part II: Structural Examples, *Computers & Structures*, vol. **84**, no. 3–4, pp. 181–95, January 2006. DOI: 10.1016/j.compstruc.2005.09.004

Milani, Gabriele and Venturini, G., Automatic Fragility Curve Evaluation of Masonry Churches Accounting for Partial Collapses by Means of 3D FE Homogenized Limit

Analysis, *Computers & Structures*, vol. **89**, no. 17–18, pp. 1628–48, September 2011. DOI: 10.1016/j.compstruc.2011.04.014

Otero, F., Oller, S., Martinez, X. and Salomón, O., Numerical Homogenization for Composite Materials Analysis. Comparison with Other Micro Mechanical Formulations, *Composite Structures*, vol. **122**, pp. 405–16, accessed August 28, 2017, from http://linkinghub.elsevier.com/retrieve/pii/S0263822314006102, April 2015. DOI: 10.1016/j.compstruct.2014.11.041

Reccia, E., Leonetti, L., Trovalusci, P. and Cecchi, A., A Multiscale/Multidomain Model for the Failure Analysis of Masonry Walls: A Validation with a Combined FEM/DEM Approach, *International Journal for Multiscale Computational Engineering*, vol. **16**, no. 4, pp. 325–43, 2018. DOI: 10.1615/IntJMultCompEng.2018026988

Ren, X., Chaurasia, A. K. and Seidel, G. D., Concurrent Multiscale Modeling of Coupling between Continuum Damage and Piezoresistivity in CNT-Polymer Nanocomposites, *International Journal of Solids and Structures*, vol. **96**, pp. 340–54, October 2016. DOI: 10.1016/j.ijsolstr.2016.05.018

Restrepo Vélez, L. F., Magenes, G. and Griffith, M. C., Dry Stone Masonry Walls in Bending-Part I: Static Tests, *International Journal of Architectural Heritage*, vol. **8**, no. 1, pp. 1–28, 2014. DOI: 10.1080/15583058.2012.663059

Roca, P., Cervera, M., Pelà, L., Clemente, R. and Chiumenti, M., Continuum FE Models for the Analysis of Mallorca Cathedral, *Engineering Structures*, vol. **46**, pp. 653–70, January 2013. DOI: 10.1016/j.engstruct.2012.08.005

Rodrigues, E. A., Manzoli, O. L., Bitencourt, L. A. G., Bittencourt, T. N. and Sánchez, M., An Adaptive Concurrent Multiscale Model for Concrete Based on Coupling Finite Elements, *Computer Methods in Applied Mechanics and Engineering*, vol. **328**, pp. 26–46, January 2018. DOI: 10.1016/j.cma.2017.08.048

Rutten, D., Galapagos: On the Logic and Limitations of Generic Solvers, *Architectural Design*, vol. **83**, no. 2, pp. 132–35, March 2013. DOI: 10.1002/ad.1568

Savalle, N., Mousavian, E., Colombo, C., and Lourenço, P. B., FAST GENERATIVE TOOL FOR MASONRY STRUCTURES GEOMETRIES, *14th Canadian Masonry Simposium*, Montréal, Canada, pp. 1–11, 2021.

Savalle, N., Vincens, É. and Hans, S., Experimental and Numerical Studies on Scaled-down Dry-Joint Retaining Walls: Pseudo-Static Approach to Quantify the Resistance of a Dry-Joint Brick Retaining Wall, *Bulletin of Earthquake Engineering*, vol. **18**, no. 2, pp. 581–606, January 2020. DOI: 10.1007/s10518-019-00670-9

Sharma, S., Silva, L. C., Graziotti, F., Magenes, G. and Milani, G., Modelling the Experimental Seismic Out-of-Plane Two-Way Bending Response of Unreinforced Periodic Masonry Panels Using a Non-Linear Discrete Homogenized Strategy, *Engineering Structures*, vol. **242**, no. December 2020, from https://doi.org/10.1016/j.engstruct.2021.112524, 2021. DOI: 10.1016/j.engstruct.2021.112524

Silva, L. C., Lourenço, P. B. and Milani, G., Nonlinear Discrete Homogenized Model for Out-of-Plane Loaded Masonry Walls, *Journal of Structural Engineering*, vol. **143**, no. 9, p. 4017099, from https://doi.org/10.1061/(ASCE)ST.1943-541X.0001831, September 1, 2017. DOI: 10.1061/(ASCE)ST.1943-541X.0001831

Smoljanović, H., Živaljić, N., Nikolić, Ž. and Munjiza, A., Numerical Analysis of 3D Dry-Stone Masonry Structures by Combined Finite-Discrete Element Method, *International Journal of Solids and Structures*, vol. **136**–**137**, pp. 150–67, April 2018. DOI: 10.1016/j.ijsolstr.2017.12.012

Sorrentino, L., D’Ayala, D., Felice, G. de, Griffith, M. C., Lagomarsino, S. and Magenes, G., Review of Out-of-Plane Seismic Assessment Techniques Applied To Existing Masonry Buildings, *International Journal of Architectural Heritage*, vol. **11**, no. 1, pp. 2–21, from https://doi.org/10.1080/15583058.2016.1237586, January 2, 2017. DOI: 10.1080/15583058.2016.1237586

Stepinac, M., Lourenço, P. B., Atalić, J., Kišiček, T., Uroš, M., Baniček, M. and Šavor Novak, M., Damage Classification of Residential Buildings in Historical Downtown after the ML5.5 Earthquake in Zagreb, Croatia in 2020, *International Journal of Disaster Risk Reduction*, vol. **56**, p. 102140, April 2021. DOI: 10.1016/j.ijdrr.2021.102140

Talebi, H., Silani, M. and Rabczuk, T., Concurrent Multiscale Modeling of Three Dimensional Crack and Dislocation Propagation, *Advances in Engineering Software*, vol. **80**, no. C, pp. 82–92, February 2015. DOI: 10.1016/j.advengsoft.2014.09.016

The Python Language Reference — Python 3.9.5 Documentation, n.d.

Trovalusci, P., Ostoja-Starzewski, M., Bellis, M. L. De and Murrali, A., Scale-Dependent Homogenization of Random Composites as Micropolar Continua, *European Journal of Mechanics - A/Solids*, vol. **49**, pp. 396–407, 2015. DOI: https://doi.org/10.1016/j.euromechsol.2014.08.010

Turco, C., Funari, M. F., Spadea, S., Ciantia, M., and Lourenço, P. B., A Digital Tool Based on Genetic Algorithms and Limit Analysis for the Seismic Assessment of Historic Masonry Buildings, *Procedia Structural Integrity*, vol. **28**, 2020.

Vandoren, B., Proft, K. De, Simone, A. and Sluys, L. J., Mesoscopic Modelling of Masonry Using Weak and Strong Discontinuities, *Computer Methods in Applied Mechanics and Engineering*, vol. **255**, pp. 167–82, March 2013. DOI: 10.1016/j.cma.2012.11.005

Vlachakis, G., Vlachaki, E. and Lourenço, P. B., Learning from Failure: Damage and Failure of Masonry Structures, after the 2017 Lesvos Earthquake (Greece), *Engineering Failure Analysis*, vol. **117**, p. 104803, November 2020. DOI: 10.1016/j.engfailanal.2020.104803